Optical and Quantum Electronics (2026) 58:107
https://doi.org/10.1007/s11082-025-08651-w

High-performance terahertz graphene biosensors employing octagonal and hybrid resonators for cancer cell detection

Saeed Heidary Kamarroodi[1] · **Javad Javidan**[1]

Received: 29 October 2025 / Accepted: 22 December 2025

Abstract
In this work, a fundamental single-band graphene-based biosensor structure is proposed, where the patterned graphene layer is designed in an octagonal geometry. Based on this configuration, dual-band absorbers are developed by integrating additional ring and plus-shaped resonators. All the proposed sensors share a simple three-layer configuration consisting of a metallic ground plane, a SiO_2 dielectric spacer, and a patterned graphene sheet functionalized by the target analyte. By optimizing the geometrical parameters and tuning the chemical potential and relaxation time of graphene, both the resonance frequencies and absorption intensity can be effectively controlled. The designed structures exhibit near-perfect absorption at their resonance bands and provide a compact and efficient platform for terahertz biosensing applications. The first proposed sensor shows a single absorption peak with 99.88% absorption and demonstrates promising results in detecting breast, cervical, and PC12 cancer cells, with the highest sensitivity of 2.14 THz/RIU observed for PC12 cancer cells. The second proposed sensor has two resonance bands, each exhibiting over 97.5% absorption, and shows notable sensitivity for detecting breast, Jurkat, and PC12 cancer cells, with the highest sensitivity of 4.21 THz/RIU observed for breast cancer at the second band. The third proposed sensor also has two resonance bands with over 98.5% absorption for each band and provides suitable sensitivity for detecting basal, cervical, and MCF-7 cancer cells, with the highest sensitivity of 1.66 THz/RIU observed for cervical cancer at the second band. The proposed technology offers a rapid and economical approach for oncological detection, enabling real-time tracking and tailored therapeutic strategies. All computational analyses were conducted using CST software.

Keywords Graphene-based biosensor · Terahertz absorption · Cancer detection · Dual-band metasurface · Biosensing performance

✉ Javad Javidan
Javidan@uma.ac.ir

[1] Department of Electrical and Computer Engineering, University of Mohaghegh Ardabili, Ardabil, Iran

Published online: 28 January 2026

1 Introduction

In recent years, biosensing has attracted considerable attention due to its vital role in healthcare, disease diagnosis, and drug development. Various sensing approaches, including mechanical and electrical methods, have been widely explored (Chalklen et al. 2020). Mechanical biosensing commonly employs structures such as micropillars (Rizzi et al. 2015), piezoelectric devices (Jandas et al. 2020), and microcantilevers (Liu et al. 2019), although these techniques often involve complex fabrication processes. In contrast, electrical biosensing detects target analytes by monitoring changes in dielectrophoretic effects (Li and Anand 2018), impedance (Nahid et al. 2020), or signal variations in field-effect transistors (Presnova et al. 2017). In both cases, analytes must be bound to the sensing element, which may compromise the integrity of biological samples. This limitation motivates the development of non-destructive sensing technologies.

Terahertz (THz) waves, positioned between the microwave and infrared spectral ranges, interact with biomolecules such as proteins, DNA, and cells via their unique vibrational modes. By analyzing alterations in THz signals, valuable insights can be gained regarding the composition, structure, and dynamics of biological specimens. Compared to ionizing radiation such as X-rays or gamma rays, THz waves possess significantly lower energy, making them safe for both samples and operators. Additionally, their non-invasive nature allows repeated measurements without damaging specimens. These properties make THz-based biosensing a promising tool for early disease detection, quality evaluation of biological materials, and drug screening. Nonetheless, the relatively large wavelength of THz waves (30–3000 μm) compared to the nanoscale dimensions of viruses, bacteria, and biomolecules limits detection sensitivity. To overcome these limitations, enhancing THz wave resonance at micro and nanoscale levels using engineered metamaterials has emerged as an effective strategy. Manipulation of electromagnetic (EM) waves across a broad spectrum from microwaves to visible light can be achieved by designing subwavelength-scale unit cells (Walser 2001; Marques et al. 2002; Chen et al. 2017).

Metamaterials are fabricated through various methods, including electron beam lithography (EBL), optical lithography, and printed circuit board (PCB) technology, tailored respectively for visible-light applications (Cao et al. 2014), THz (Zhang, et al. 2017), and microwave (Zhang et al. 2022a). Unit cell architectures such as gammadion shapes (Zhang et al. 2014), fishnet patterns (Valentine et al. 2008; Kafesaki et al. 2007), and split-ring resonators (Smith et al. 2000; Linden et al. 2004; Zhang, et al. 2012) are employed to induce specific EM resonances. These engineered resonances enable extraordinary EM phenomena, including extraordinary transmission (Zhang et al. 2008; Liu et al. 2009; Liu et al. 2024), strong optical activity (Plum et al. 2009; Valev et al. 2013; Zhang et al. 2021), perfect absorption (Song et al. 2017; He et al. 2024), and negative refraction (Shelby et al. 2001; Shalaev 2007). Such properties open possibilities for diverse applications such as polarization conversion (Grady et al. 2013; Gansel et al. 2009; Zhang et al. 2017), superlenses (Zhang and Liu 2008; Jacob et al. 2006; Poddubny et al. 2013), and invisibility cloaking (Schurig et al. 2006; Cai et al. 2007; Valentine et al. 2009). Recently, two-dimensional metamaterials, or metasurfaces, have attracted significant attention due to their ability to precisely control EM wavefronts, facilitating functions such as imaging (Zheng et al. 2015; Ni et al. 2013; Kawata et al. 2008), beam shaping (Zhang et al. 2022b), and flat-lens focusing (Aieta et al. 2012; Khorasaninejad et al. 2016).

A growing body of recent research has underscored the transformative potential of graphene-integrated terahertz platforms for advanced sensing and biomedical diagnostics. One review highlights graphene-based terahertz metasurfaces and their pivotal role in biochemical sensing, emphasizing the unique advantages of terahertz waves, the increasing demand for higher sensitivity, and the underlying sensing mechanisms of such devices. It presents concrete examples including the detection of proteins, nucleic acids, and chemical molecules, offers a comparative analysis of graphene against nanomaterials, silicon, and metals, and concludes with a summary of performance metrics, current limitations, and prospective strategies for improvement (Bi et al. 2023). Another review focuses on graphene-based nanomaterials, which have attracted considerable attention owing to their exceptional physical, chemical, biological, and optoelectronic properties. It particularly emphasizes their application in developing highly sensitive biosensors for the rapid detection of pathogens and biomolecules, summarizing recent advances while critically addressing challenges related to synthesis and real-world deployment (Baruah et al. 2024). A third contribution, presented as a mini-review, examines the roles of graphene and its oxidized derivative, graphene oxide, in diverse sensor technologies. It notes graphene's outstanding thermal and electrical conductivity, which render it suitable for electrical, strain, and toxic gas sensors, while highlighting how the oxygen-containing functional groups in graphene oxide extend its utility to gas sensing, biosensing, and electrochemical detection. The review systematically outlines the efficiency, selectivity, advantages, and inherent limitations of both materials (Bose, et al. 2023). Recent works by Khodadadi et al. have demonstrated the adaptability of graphene-based terahertz metamaterial absorbers in diverse sensing contexts. These studies present a range of symmetric, polarization-insensitive designs employing octagonal rings, wheel-like elements, and corner triangles that enable strong, tunable absorption across single, dual, and triple bands. Such structures have been successfully applied to both biomedical diagnostics (including cancer and malaria detection) and environmental monitoring (notably for trace gas sensing). These advancements highlight the broad utility of graphene metasurfaces as highly responsive and reconfigurable platforms for refractive-index–based sensing in the terahertz regime (). In this study, a conceptual refinement in resonator engineering is introduced, wherein compact central elements, specifically a ring or a plus-shaped resonator, are integrated into a high-symmetry octagonal graphene platform. This hybrid strategy enables spatially decoupled dual-band plasmonic responses within a single, polarization-insensitive, and fabrication-compatible unit cell, thereby making simultaneous multi-analyte cancer detection possible without structural complexity.

In conclusion, this study presents three unique terahertz (THz) graphene-based metamaterial absorber designs for sensing applications. The first design features a graphene sheet shaped into an octagonal ribbon, placed atop gold and SiO_2 substrates, resulting in a single-band absorption profile. By keeping this foundational structure and introducing two additional configurations, a ring and a plus-shaped element at its center, the absorption characteristics shift from one band to two distinct bands for each modified sensor. All three designs exhibit high sensitivity and strong spectral selectivity. However, the two added structures also offer polarization-independent performance, while the base structure does not. The straightforward nature of these configurations simplifies fabrication and enhances their potential for biomedical use. Furthermore, the absorption bands of these sensors can be dynamically controlled by tuning graphene's electrochemical potential and relaxation time, removing the necessity for structural redesign. Simulations conducted with CST Microwave

Studio confirm the high efficiency and tunability of all three sensors. These findings indicate that the proposed designs offer promising, cost-efficient, and effective platforms for THz-based biomedical sensing.

2 Device architecture and computational simulation

2.1 Theoretical modeling of graphene conductivity

The numerical simulation of monolayer graphene is performed using the surface conductivity model, in which the conductivity $\sigma(\omega, \tau, \mu_c)$ is evaluated through the Kubo formalism (Thongrattanasiri et al. 2012).

$$\sigma\left(\omega, \tau, \mu_c, T\right) = \sigma_{\text{inter}}\left(\omega, \tau, \mu_c, T\right) + \sigma_{\text{intra}}\left(\omega, \tau, \mu_c, T\right) \tag{1}$$

$$\sigma_{\text{inter}}\left(\omega, \tau, \mu_c, T\right) = -j\frac{e^2}{4\pi\hbar}\ln\left(\frac{2\mu_c + \left(\omega - j\tau^{-1}\right)\hbar}{2\mu_c - \left(\omega - j\tau^{-1}\right)\hbar}\right) \tag{2}$$

$$\sigma_{\text{intra}}\left(\omega\ ,\ \tau,\ \mu_c,\ T\right) = -j\frac{e^2\ K_B\ T}{\pi\ \hbar^2\ \left(\omega\ - j\ \tau^{-1}\right)}\left[\frac{\mu_c}{K_B\ T} + 2\ \ln\left(\exp\ \left(-\frac{\mu_c}{K_B\ T}\right) + 1\right)\right] \tag{3}$$

In this framework, the overall surface conductivity of graphene is described as the sum of two distinct terms: the interband contribution, originating from electronic transitions across different energy bands, and the intraband contribution, arising from carrier transitions within the same band. The incident electromagnetic wave is characterized by its angular frequency ω, while K_B represents the Boltzmann constant. The reduced Planck constant is defined as $\hbar$=h/2π, and the absolute temperature is fixed at 300 K. The elementary charge is denoted by e. A key parameter in this model is the carrier relaxation time τ, which can be expressed in terms of the carrier mobility μ, the Fermi velocity V_f, and the Fermi level μ_c, according to $\tau = \mu \cdot \mu_c / eV_f^2$. Within the terahertz frequency range, the photon energy satisfies the relations $\hbar_\omega \ll \mu_c$ and $\mu_c \gg K_B T$, indicating that the photon energy is much smaller than the Fermi level. Under these assumptions, the effect of interband transitions becomes negligible, and the conductivity reduces to a quasi-Drude form (Thongrattanasiri et al. 2012).

$$\sigma\left(\omega, \tau, \mu_c\right) = \frac{je^2\mu_c}{\pi\hbar^2\left(\omega + j\tau^{-1}\right)} \tag{4}$$

In practice, the electrical properties of graphene, particularly its chemical potential (μ_c) and carrier relaxation time (τ), can be dynamically controlled through external means such as electrostatic gating or chemical doping. A top-gate configuration, as illustrated in typical graphene-based THz absorbers (), applies a DC bias voltage (V_g) across a thin dielectric (e.g., SiO_2 or poly-silicon), which shifts the Fermi level (μ_c) according to Eq. (5).

$$V_g = \frac{q_e\mu_c^2 h}{\pi\hbar^2 v_F^2 \varepsilon_0 \varepsilon_r} \tag{5}$$

where h is the dielectric thickness, ε_r its relative permittivity, and v_F the Fermi velocity. This gating directly modulates the surface conductivity via Eq. (4), enabling real-time tuning of the absorption frequency without altering the physical geometry. Concurrently, the relaxation time τ, which governs Drude damping and thus the resonance linewidth, is linked to carrier mobility (μ) and μ_c through $\tau = \mu \cdot \mu_c / e \cdot v_F^2$ (Khodadadi et al. 2023a, 2023b, 2025a; Razani et al. 2022).

Any process that affects scattering (e.g., phonon interactions, impurity doping, or surface roughness) alters τ. A reduction in τ broadens the absorption peak, lowers the quality factor, and diminishes peak absorption, while a higher τ sharpens the resonance and enhances sensing resolution. Therefore, precise control of both gating and material purity is essential for maintaining high-performance absorption in practical THz biosensing.

2.2 Development and modeling of multi-resonant structures

In this study, three distinct perfect absorption structures are proposed. Each of these structures is composed of three layers. The bottom layer consists of a gold cube with lateral dimensions of W × W (W = 2.5 μm) and a thickness of 0.3 μm, where the gold exhibits an electrical conductivity of $\sigma_{Au} = 4.7 \times 10^7$ S/m (Tian et al. 2021). This conductive layer is responsible for completely suppressing the transmission of electromagnetic waves through the structure. The middle layer is a cube with identical lateral dimensions (W × W) and a thickness of 4.6 μm, made of SiO_2, which possesses a relative permittivity of $\varepsilon_r = 3.9$ (Chen and Alu 2011). The bottom two layers, gold and SiO_2, are identical across all three structures. However, the design and properties of the top graphene layer differ for each structure, leading to unique absorption responses in different frequency bands. The top layer in all structures is composed of graphene with a thickness of 1 nm, operating at a temperature of 300 K. The other characteristics and parameters of the graphene layers, which vary between the structures and are responsible for their distinctive electromagnetic absorption behaviors, are summarized in Table 1. For all proposed designs, the structures are modeled as periodic unit cells in the x–y plane, while open boundary conditions are applied along the vertical direction. Within the scope of electromagnetic field theory, the absorption A(ω) is defined as follows (Zhao et al. 2018):

$$A(\omega) = 1 - R(\omega) - T(\omega) = 1 - |s_{11}(\omega)|^2 - |s_{21}(\omega)|^2 \tag{6}$$

Here, $R(\omega) = |s_{11}(\omega)|^2$ represents the reflection coefficient, and $T(\omega) = |s_{21}(\omega)|^2$ denotes the transmission coefficient. In all three proposed structures, a metallic (gold) layer is employed as the bottom layer, effectively preventing wave transmission. Therefore, $T(\omega) = |s_{21}(\omega)|^2 = 0$. Furthermore, reflectance is significantly reduced due to the constructive interference occurring within the Fabry–Perot (F–P) cavity formed by the dielec-

Table 1 The most important parameters of the proposed absorber structures for achieving the best results

Structure	Parameters			
Proposed I	μ_c(ev)	τ (ps)	a (μm)	m (μm)
	0.4	3	1.25	0.6
Proposed II	μ_c(ev)	τ (ps)	K (μm)	L (μm)
	0.4	2.7	0.2	0.9
Proposed III	μ_c(ev)	τ (ps)	o (μm)	i (μm)
	0.4	2.7	0.38	0.1

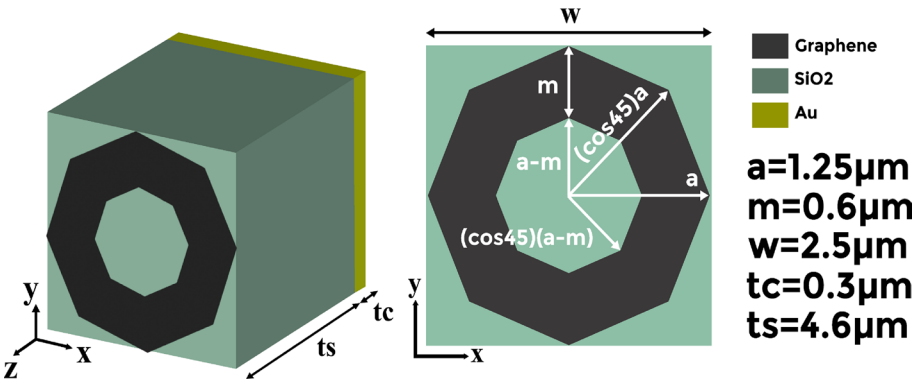

Fig. 1 The upper surface and schematic diagram of the first proposed absorber structure

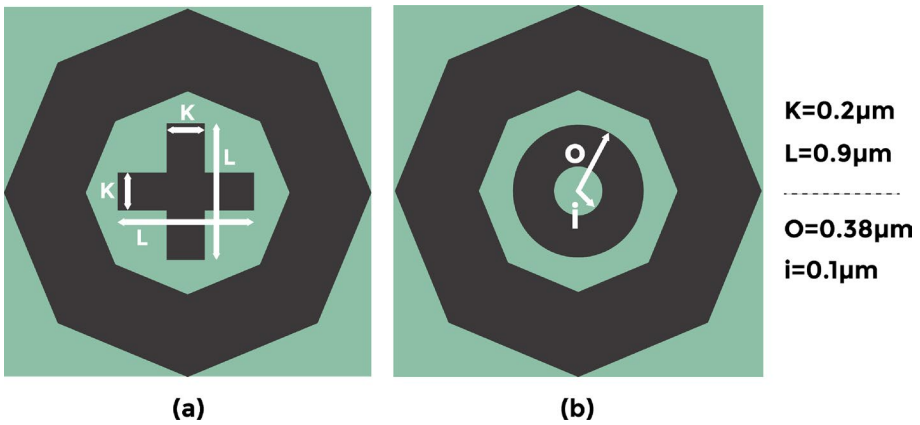

Fig. 2 Upper surface of **a** The second proposed absorber **b** The third proposed absorber

tric layer. Combined with enhanced electromagnetic field oscillations generated within the graphene layer, this mechanism results in near-zero reflection, i.e., $\mathrm{R}(\omega) = |s_{11}(\omega)|^2 = 0$, thereby achieving complete absorption with A(ω) = 1. This demonstrates the maximum absorption efficiency across all three structures. It should also be noted that during the CST simulations, the frequency range was set from 0.1 to 10 THz, while the graphs presented here utilize specific frequency ranges according to the requirements.

Figure 1 shows the first absorber structure, which also serves as the base structure, along with its dimensions. In Fig. 2, the graphene pattern on the top layer of this base structure is modified by adding a plus-shaped sign and a ring at the center to form the second and third structures. All other dimensions and specifications are identical to those of the first absorber. Figure 3 presents the output waveform of all three absorbers.

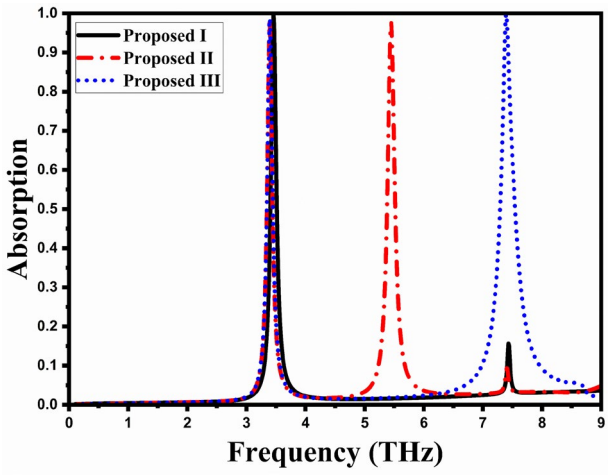

Fig. 3 Absorption waveforms of the proposed absorbers

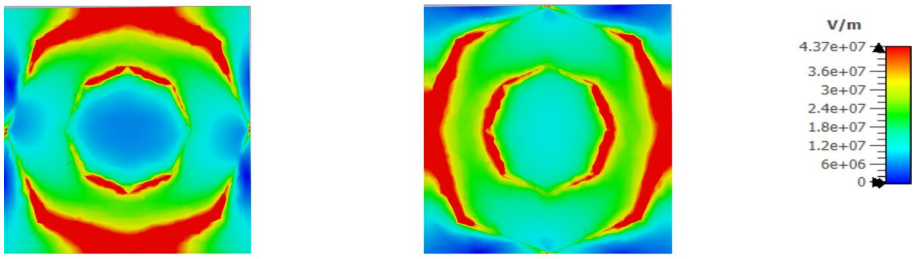

Fig. 4 Electric field [Real (Ez)] distributions at normal incidence for **a** TE and **b** TM polarizations of the first proposed structure at 3.458THz

3 Electric field distribution under TE and TM polarizations

In the designed absorbers, the gold ground layer blocks transmission, while a single functional layer composed of SiO_2 and graphene minimizes reflection through interference effects. Simultaneously, surface plasmons excited at the metal–dielectric interface interact strongly with the incident light. At localized surface plasmon resonance (LSPR), the electromagnetic field becomes confined within nanoscale regions. These localized fields are extremely sensitive to the dielectric environment and the geometry of nanostructures, making the system highly suitable for sensing applications. Figure 4 presents the electric field distributions for TE and TM polarized waves at resonance frequencies, calculated at the top surface of the first proposed absorber structure, which serves as the base structure. These results clearly confirm the plasmonic behavior of the absorber under different polarizations.

As shown in Fig. 4, under TE and TM modes, the electric field distributions are mainly concentrated around the outer, inner, and edge regions of the octagonal strip. In continuation, by adding the plus-shaped element and the ring to the basic structure, the first resonance frequency appears in both modified structures, which is approximately close to that of the basic design. However, the second resonance frequencies are generated in the second

and third structures. These newly formed resonances can be identified from the field distribution plots, resulting from the excitation of surface plasmons at the metal–dielectric interfaces. Figure 5 shows the electric field distributions of the second absorber under TE and TM polarized waves at its resonance frequencies.

It is observed from Figs. 5a and 5b that the electric field distributions under TE and TM polarized waves at 3.389 THz of the second absorber are quite similar to those of the base structure, exhibiting relatively low field intensities around the plus-shaped pattern. At 5.45 THz, as shown in Fig. 5c, d, the electric field intensities around the plus-shaped pattern are significantly higher for both TE and TM modes, especially in the vicinity of the added plus-shaped pattern.

Figure 6 shows the electric field distributions of the third absorber under TE and TM polarized waves at its resonance frequencies. All the analyses presented for the electric field distributions under TE and TM polarizations of the second absorber also apply to the third absorber, with both structures exhibiting similar behavior and field distribution patterns in comparison to the base structure.

4 Equivalent circuit modeling of the proposed terahertz absorber

Various analytical frameworks have been employed in the literature to validate the performance of graphene-based terahertz absorbers, including transmission line modeling and coupled mode theory, which provide complementary insights into impedance matching and resonance dynamics (Khatami et al. 2025a, 2025b). This section presents the equivalent circuit modeling of the proposed terahertz absorber. The overall configuration of the circuit and the role of each component are described. Then, the reflection coefficient (S_{11}) obtained

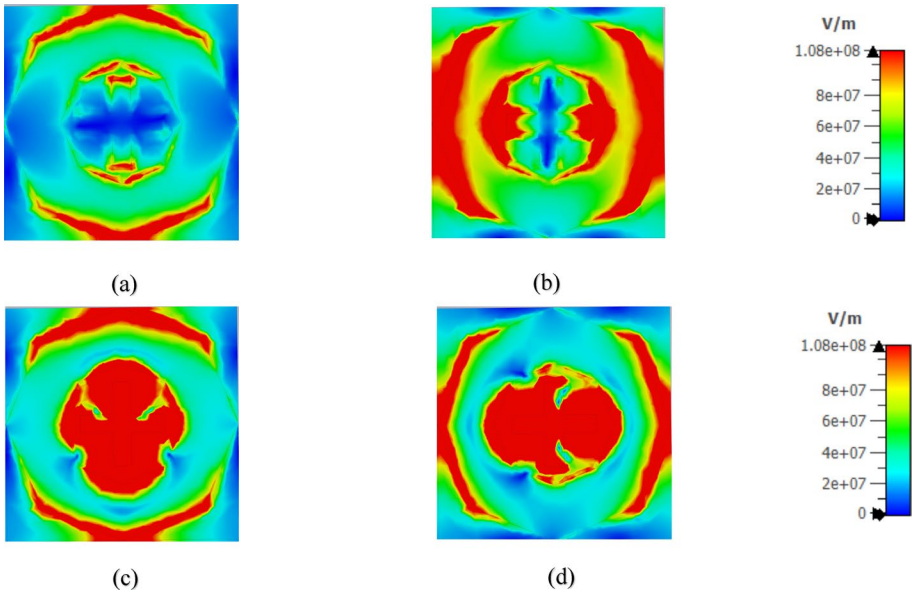

Fig. 5 Electric field [Real (Ez)] distributions at normal incidence of TE waves: (**a**, **c**) at 3.389 THz, 5.45 THz; and of TM waves: (**b**, **d**) at 3.389 THz, 5.45 THz, for the second proposed absorber structure

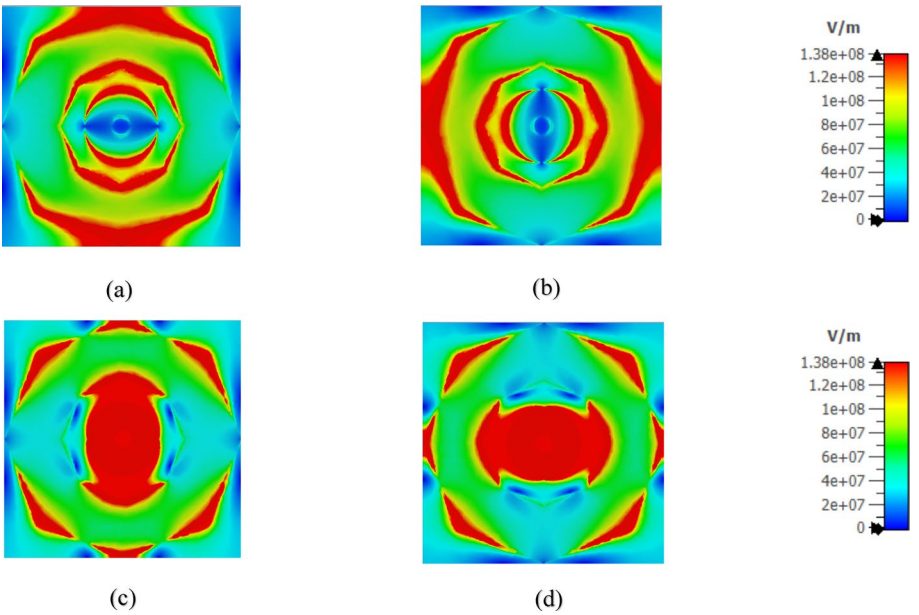

Fig.6 Electric field [Real (Ez)] distributions at normal incidence of TE waves: (**a**, **c**) at 3.399 THz, 7.392 THz; and of TM waves: (**b**, **d**) at 3.399 THz, 7.392 THz, for the third proposed absorber structure

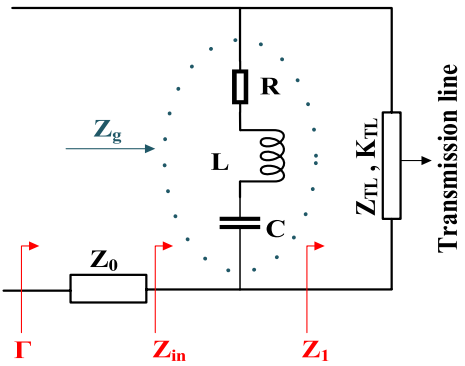

Fig. 7 Representation of the equivalent circuit for the first proposed absorber

from the circuit model is analyzed to verify the resonance behavior within the desired frequency range. Furthermore, the mathematical formulations for calculating the input impedance, propagation constant, and equivalent RLC parameters are derived. This analysis aims to optimize the absorber's performance by utilizing the tunable electromagnetic properties of graphene layers.

As illustrated in Fig. 7, the proposed equivalent circuit model represents the gold substrate as a short-circuited transmission line with zero impedance ($Z_{AU}=0$). The intermediate dielectric layer, referred to as the spacer, is modeled as a transmission line characterized by impedance Z_{TL} and electrical length E_{TL} ($E_{TL}=2\times K_{TL}\times t_s$).

The octagonal graphene pattern (first proposed structure) is represented by an RLC branch, where Z_g denotes the corresponding impedance. Moreover, in this model, the

impedance of free space is defined as $Z_0 == 120\pi \approx 377\Omega$. The input surface impedance of the proposed equivalent circuit can be calculated using the following relations (Rafighirani and Javidan 2025).

$$Z_1 = jZ_{TL}tan(K_{TL}t_s) \tag{7}$$

$$K_{TL} = 2\pi f\sqrt{\varepsilon_0\varepsilon_r\mu_0} \tag{8}$$

$$Z_{TL} = \sqrt{\mu_0/\varepsilon_0\varepsilon_r} \tag{9}$$

$$Z_g(f) = R + jX_g = R + j\left(2\pi fL - \frac{1}{2\pi fC}\right) = \frac{1}{\sigma_g(f)} \tag{10}$$

$$Z_{in} = \frac{Z_1.Z_g}{Z_1 + Z_g} \tag{11}$$

Here, K_{TL} and ε_r denote the wavenumber and the relative permittivity of the dielectric spacer layer, respectively. Moreover, ε_0 and μ_0 represent the permittivity and permeability of free space. The equivalent resistance (R), inductance (L), and capacitance (C) of the graphene branch can be determined using the following relations (Rafighirani et al. 2025a).

$$R = \frac{Kw^2}{\pi S^2}\frac{\hbar^2}{e^3\mu_c\tau}, L = \frac{Kw^2}{\pi S^2}\frac{\hbar}{e^3\mu_c}, C = \frac{\pi^2S^2}{w^2k}\frac{\varepsilon}{q_1} \tag{12}$$

Here, ε represents the permittivity of the dielectric layers surrounding the graphene on both sides, while q_1 denotes the first eigenvalue obtained from the governing equation of the surface current distribution on the octagon graphene pattern. Furthermore, the parameters K and S can be determined following the procedure outlined in Ref. (Barzegar-Parizi et al. 2015). Based on these definitions, the reflection coefficient (Γ) of the structure can be evaluated using the expression below.

$$\Gamma = \frac{Re(Z_{in}) - Z_0}{Re(Z_{in}) + Z_0} \tag{13}$$

Based on the proposed equations, the extracted values for the equivalent circuit components are as follows: Z_{TL}=190.765 Ω, E_{TL}=37.634923∘, R=46.5 Ω, L=97.8399e-11 H and C=2.0359248e-17 F.

In Fig. 8, the S_{11} parameter of the first proposed absorber is plotted using ADS software after optimizing the equivalent circuit element values, and it is compared with the simulated S_{11} obtained from CST software. As observed, there is a strong agreement between the circuit model and the simulated results, which validates the accuracy of the first proposed sensor's design. Similarly, the equivalent circuit model can be derived for the second and third proposed structures following the same approach.

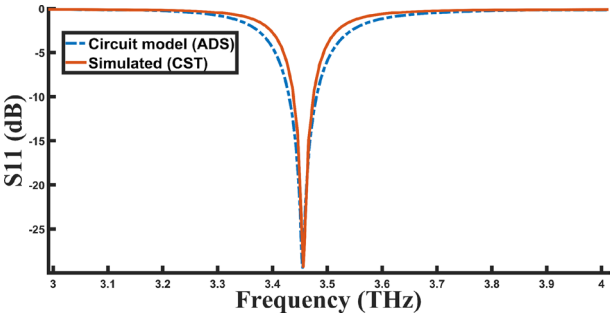

Fig. 8 S 11 spectra obtained from simulations and the circuit model of the first proposed structure

5 Design methodology of the proposed structures

The three proposed absorbers each consist of three functional layers. The bottom metallic layer acts as a perfect reflector in the terahertz regime, completely suppressing transmission and confining all incident electromagnetic energy within the structure. Above it, a dielectric spacer establishes a resonant cavity between the metallic reflector and the patterned graphene surface, enabling constructive interference and strong field confinement that substantially enhance light–matter interaction. The top layer features patterned graphene, selected for its exceptional tunability and ability to support localized surface plasmon resonances in the terahertz frequency range. By carefully tailoring the geometrical parameters and intrinsic properties of graphene, the absorption spectrum can be engineered to exhibit multiple distinct peaks with nearly perfect efficiency.

The geometric and electrochemical parameters of the proposed absorbers were selected through a systematic design process grounded in both physical feasibility and performance-driven optimization. The chemical potential (μ_c) and carrier relaxation time (τ) of graphene were constrained to experimentally achievable ranges reported for high-quality CVD-grown graphene at room temperature: $\mu c = 0.3–0.6$ eV and $\tau = 2–6$ ps, corresponding to carrier mobilities of 10^4–10^5 $cm^2/V \cdot s$(Thongrattanasiri et al. 2012; Huang et al. 2022). Within this space, values yielding absorption > 97.5% and maximum refractive-index sensitivity were identified via iterative simulation. The final choices ($\mu_c = 0.4$ eV, $\tau = 2.7–3$ ps) represent an optimal balance between strong plasmonic response and realistic device operation. Similarly, the geometric parameters (e.g., a, m, K, L, o, i) were swept within subwavelength limits consistent with the unit cell size ($W = 2.5$ μm λ in 0.1–10 THz), guided by the design strategies reported in recent theoretical and simulation-based studies on graphene-based THz resonators (Pilehroudi et al. 2025; Rafighirani et al. 2025b). Specifically, feature sizes were restricted to 0.1–1.5 μm, a range proven to support robust localized surface plasmon resonances in the terahertz regime while remaining compatible with standard photolithography. The optimal values listed in Table 1 were selected based on peak absorption magnitude, resonance stability, and fabrication practicality, ensuring that the resulting designs are both high-performing and realizable.

A key parameter used to evaluate the sensing efficiency of metasurface-based devices is the quality factor (Q-factor), expressed as:

$$Q = f/FWHM \tag{14}$$

Where f represents the resonance frequency and FWHM corresponds to the full width at half maximum of the resonance peak. A larger Q-factor implies a narrower resonance linewidth, which translates to enhanced sensing precision. The summarized absorption data for the designed structures are listed in Table 2. As evident, the absorption is close to 100% across all resonance bands, confirming nearly ideal absorption behavior. Moreover, the obtained Q-factor and FWHM values demonstrate excellent performance, highlighting the capability of these absorbers for potential applications in frequency-selective telecommunications components and high-performance biosensing platforms.

One of the crucial factors in determining the parameters of an absorber, particularly for the graphene-based design, is the absorption efficiency across different frequencies. In the first proposed absorber structure, these parameters include μc, τ, and other geometric factors. To identify the optimal values, a parameter sweep is conducted. Figure 9 illustrates the absorption performance of the first proposed structure as these parameters vary.

According to Fig. 9, the parameter values listed in Table 1 are clearly chosen based on the high absorption performance of the structure. The same procedure is applied to the second and third proposed absorber structures, with their results presented in Figs. 10 and 11, respectively.

6 Proposed structures for cancer cell biosensing

Refractive index–based sensors operate by detecting variations in the optical properties of the sensing medium induced by interactions with biological analytes. When a biological sample, such as a cancerous tissue, is placed on the sensor surface, it alters the local refractive index, leading to measurable shifts in resonance characteristics such as frequency, wavelength, or amplitude. Monitoring these variations enables quantitative analysis and accurate identification of biological conditions. The sensitivity **(S)** of the sensor is defined as the ratio of the resonance frequency shift to the change in the refractive index of the surrounding environment and can be expressed as

$$S = (\Delta f)/\Delta n)\, THZ/RIU \tag{15}$$

Table 2 Resonance Frequencies, Full Width at Half Maximum (FWHM), and Q-Factor for the Proposed Structures

Structure	Absorption band	Max. Absorption Freq.(THz)	Maximum Absorption(%)	FWHM (THz)	Q-factor
Proposed I	First band	3.458	99.88	0.1298	26.64
Proposed II	First band	3.389	97.79	0.1163	29.14
	Second band	5.45	97.51	0.1643	33.17
Proposed III	First band	3.399	98.59	0.1170	29.05
	Second band	7.392	99.85	0.3373	21.91

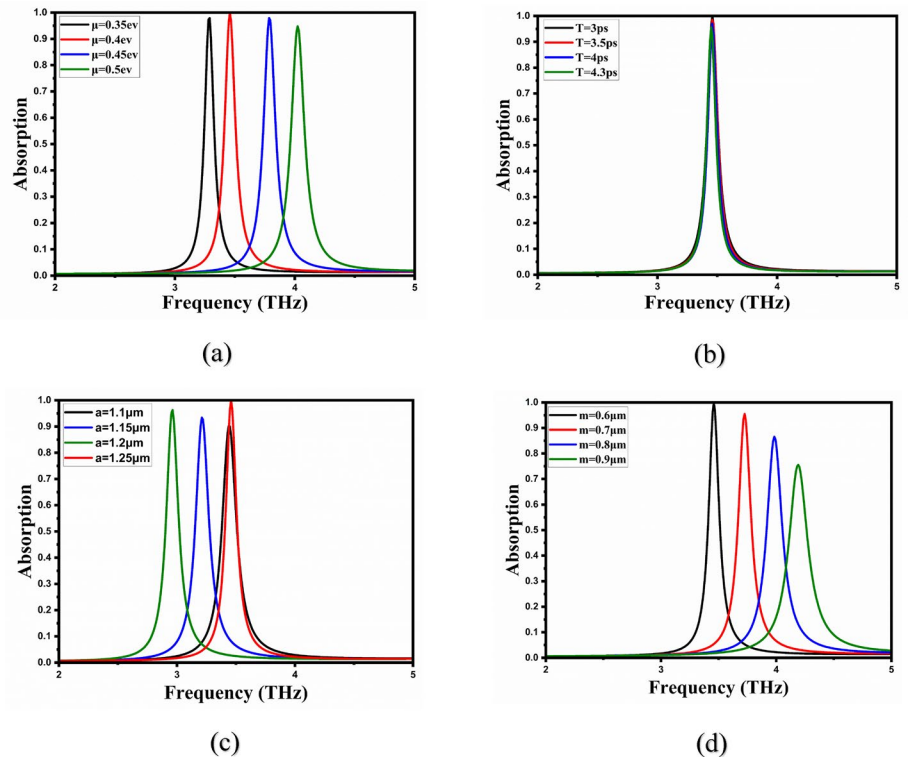

Fig. 9 **a** Chemical potential variation. **b** Relaxation time variation. **c** a parameter variation. **d** m parameter variation

Where Δf represents the resonance frequency shift and Δn denotes the variation in the refractive index (Wang et al. 2023). This parameter serves as a critical indicator of the sensor's precision and overall performance, particularly in biosensing and medical diagnostic applications. According to Cheng et al. (2020), cancerous tissues exhibit distinct refractive indices due to their higher protein concentrations compared to normal tissues. Therefore, in this work, instead of analyzing general refractive index variations, several types of cancer cells with their specific refractive indices were considered as analytes. In the simulations, analyte layers with dimensions of W × W (W = 2.5 μm) and thicknesses of 0.6 μm, 0.615 μm, and 0.615 μm were placed on the graphene layer in the first, second, and third proposed sensor structures, respectively. Since cancer cells possess higher refractive indices than healthy ones, the three proposed biosensor structures can effectively distinguish between various cancer types by tracking shifts in resonance frequency (Tables 3, 4, 5) (Huang et al. 2022; Parvin et al. 2021). The obtained results confirm that all three designs exhibit high accuracy and efficiency, demonstrating strong potential for future biomedical sensing applications.

The selection of these analyte thicknesses is based on established principles and consistent with recent literature(Razani et al. 2022; Rafighirani et al. 2025a; Khodadadi et al. 2025b; Fu et al. 2024; Zhang et al. 2023). Previous studies have shown that the frequency shift increases with analyte thickness up to the evanescent field penetration depth, which is typically a few hundred nanometers to a few micrometers, beyond which the response satu-

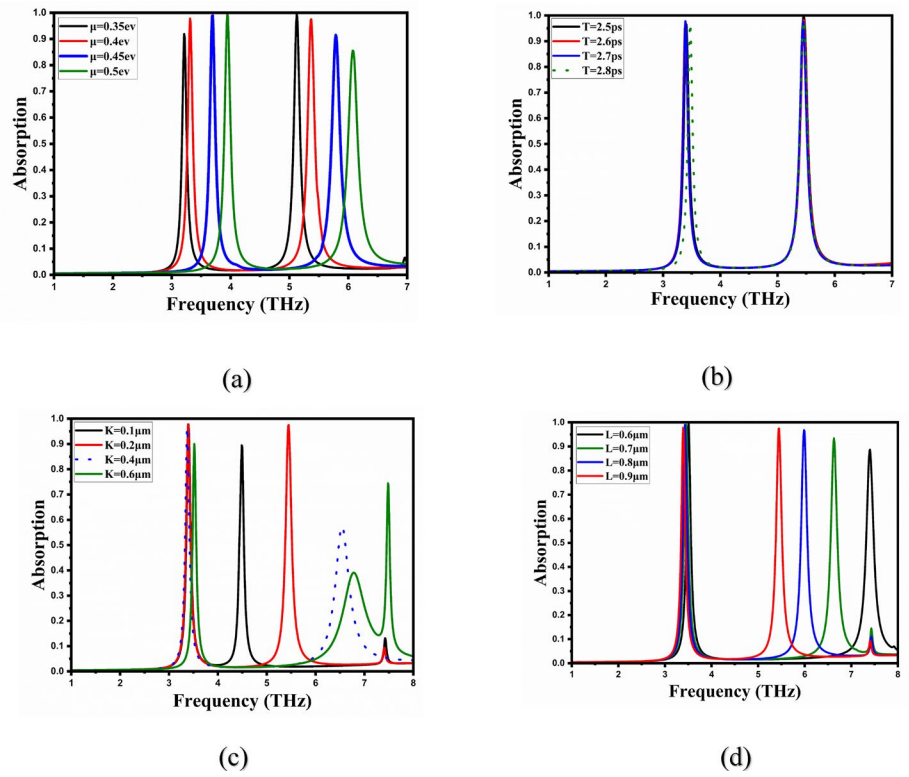

Fig. 10 **a** Chemical potential variation. **b** Relaxation time variation. **c** K parameter variation. **d** L parameter variation

rates. Only the portion of the analyte within the evanescent field effectively interacts with the localized plasmonic mode. Therefore, choosing thicknesses of 0.6 μm and 0.615 μm ensures strong field–analyte coupling and maximized sensitivity, while thicker layers provide no further improvement and may even reduce sensing efficiency. This approach is widely adopted in terahertz biosensor design.

As presented in Tables 3, 4, 5, the results of the proposed biosensors demonstrate their sensitivity to different types of cancer cells. Each cancer type is characterized by two refractive indices, one corresponding to the healthy cell and the other to the cancerous cell. To calculate the sensitivity, the refractive index of the healthy cell was first considered as the reference state, and the absorption spectra were obtained for this condition. Then, the refractive index was adjusted according to the value corresponding to the cancerous cell, and the shift in resonance peaks relative to the reference state was determined. The difference between the resonance frequencies of the cancerous and healthy cells was then divided by the refractive index difference between these two states, and the sensitivity was calculated according to Eq. (15). This method provides a precise evaluation of the biosensor's response to dielectric variations caused by cancerous transformations in biological tissues.

According to Tables 3–5, all the proposed structures exhibit strong sensitivity in detecting various types of cancer cells. The first structure demonstrates its highest sensitivity of

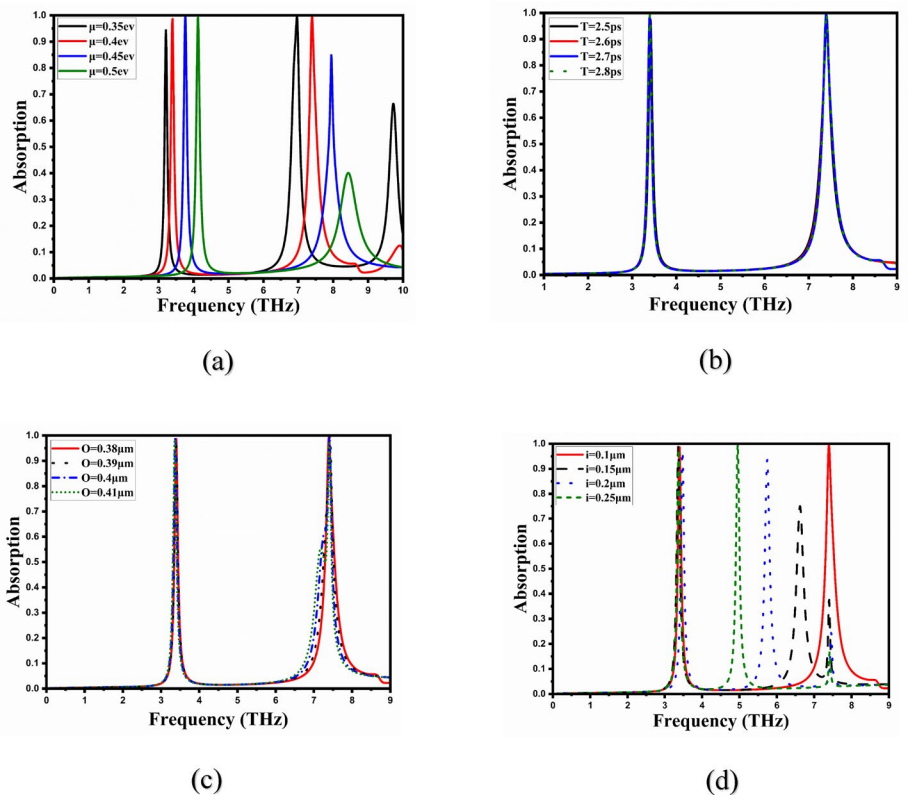

Fig. 11 **a** Chemical potential variation. **b** Relaxation time variation. **c** O parameter variation. **d** i parameter variation

Table 3 The first proposed biosensing structure to a variety of cell types, including both healthy and cancerous cells

Cell name	Cell's status	RI	Freq (THz)	Sensitivity (THz/RIU)
Breast cell	Normal	1.399	3.171	Ref
	Cancer	1.385	3.191	1.42
Cervical cell	Normal	1.368	3.25	Ref
	Cancer	1.392	3.211	1.625
PC-12	Normal	1.381	3.211	Ref
	Cancer	1.395	3.181	2.14

2.14 THz/RIU for detecting PC-12 cancer cells. In the second structure, satisfactory and consistent results are achieved across both resonance bands; however, the highest sensitivity of 4.21 THz/RIU is observed in the detection of breast cancer, corresponding to the second resonance band. For the third structure, the best sensitivity value of 1.66 THz/RIU is obtained for cervical cancer detection, which also occurs in the second resonance band.

Although Design 1 exhibits the highest single-band sensitivity (2.14 THz/RIU for PC-12 cells), Designs 2 and 3 not only match but even surpass this performance in their second resonance bands for instance, Design 2 achieves 4.21 THz/RIU for breast cancer detection.

Table 4 The second proposed biosensing structure to a variety of cell types, including both healthy and cancerous cells

			Band I		Band II	
Cell name	Cell's status	RI	Freq (THz)	Sensitivity (THz/RIU)	Freq (THz)	Sensitivity (THz/RIU)
Breast cell	Normal	1.399	3.151	Ref	4.935	Ref
	Cancer	1.385	3.161	0.71	4.994	4.21
Jurkat cell	Normal	1.367	3.191	Ref	5.024	Ref
	Cancer	1.39	3.171	0.86	4.994	1.30
PC-12	Normal	1.381	3.211	Ref	5.034	Ref
	Cancer	1.395	3.191	1.42	4.994	2.85

Table 5 The third proposed biosensing structure to a variety of cell types, including both healthy and cancerous cells

			Band I		Band II	
Cell name	Cell's status	RI	Freq (THz)	Sensitivity (THz/RIU)	Freq (THz)	Sensitivity (THz/RIU)
Basal cell	Normal	1.36	3.171	Ref	6.876	Ref
	Cancer	1.38	3.151	1	6.847	1.45
Cervical cell	Normal	1.368	3.141	Ref	6.857	Ref
	Cancer	1.392	3.132	0.37	6.817	1.66
MCF-7	Normal	1.36	3.171	Ref	6.876	Ref
	Cancer	1.401	3.161	0.24	6.827	1.19

More importantly, the dual-band nature of these modified structures enables simultaneous, multi-analyte sensing, while their symmetric geometry ensures polarization independence a critical advantage for practical biomedical applications where polarization control is unfeasible. Thus, Designs 2 and 3 are not redundant variants but complementary architectures that enhance functional versatility without compromising sensitivity.

In the proposed structures, the results of resonance frequency shifts as a function of refractive index variations from 1.0 to 1.4 in steps of 0.1 along with the fitted curves are reported (Fig. 12). These results confirm a linear relationship between the refractive index changes and the corresponding resonance frequency shifts, demonstrating the high stability and reliability of the proposed sensors.

A detailed performance comparison between the proposed metamaterial absorbers and previously reported designs is presented in Table 6. This comparison highlights key parameters such as the operational frequency range, number of absorption resonances, and sensitivity. The results demonstrate that the proposed absorbers offer superior performance for terahertz applications, surpassing earlier designs in several aspects.

7 Implementation and fabrication steps of the graphene metastructure

The fabrication procedure starts with the deposition of a thin gold layer that functions as the reflective ground plane and bottom electrode. Next, a SiO_2 dielectric film is grown on the gold surface via a physical vapor deposition (PVD) technique. A single-layer gra-

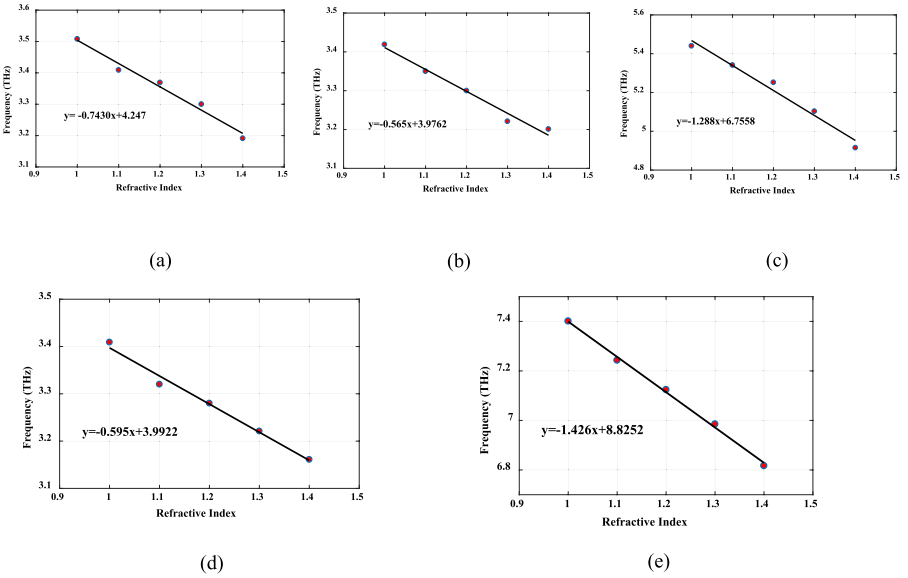

Fig. 12 Resonance frequency shifts as a function of refractive index variations for the proposed sensor structures: **a** First structure, (**b**–**c**) First and second resonance bands of the second structure, and (**d**–**e**) First and second resonance bands of the third structure

Table 6 A comparative evaluation of the present work with previously published studies

References	Geometry	Max. Absorption Freq. (THz)	Max. Absorption numbers	Max. Sensitivity (THz/RIU)
Zhang et al. (2023)	Au-PTFE(Teflon)-Au	0.73–2.2	2	0.319–1.015
Zhao and Meng (2025)	Si-Sio2-Ag	1.2–1.42	2	0.114–0.321
Lu et al. (2022)	Au- PTFE(Teflon)	1.04–2.95	2	0.309–0.730
Anwar (2023)	Au-Polyamide-Au	1.355–2.785	2	0.085–0.735
Fu et al. (2024)	Graphene-Topas-Au	2.58–6.07	2	0.714–1.627
Shangguan et al. (2022)	Graphene-Sio2-Au	5.664–8.062	2	0.875–0.775
Khodadadi et al. (2025b)	Graphene-Sio2-Si-Au	4.3–7.35	2	0.57–1.15
Wekalao et al. (2025)	Graphene-Silver-Sio2	1.212	1	1
Kumar et al. (2025)	Graphene-Sio2-Au	2.24–3.54	2	1.094–1.029
Mamoun et al. (2025)	Au-Polyamide-Au	1.99–2.7	2	0.6–0.8
Proposed I	Graphene-Sio2-Au	3.458	1	2.14
Proposed II	Graphene-Sio2-Au	3.389–5.45	2	1.42–4.21
Proposed III	Graphene-Sio2-Au	3.399–7.392	2	1–1.66

phene sheet is subsequently transferred onto the SiO_2 substrate. The desired pattern is then defined through standard photolithography followed by precise etching. The same process is employed for the realization of all three proposed sensor configurations. In the final structure, a multilayer stack comprising a gold reflector, a SiO_2 dielectric layer, and a patterned graphene sheet is obtained, as depicted in Fig. 13.

graphene sheet is obtained, as depicted in Figure 13.

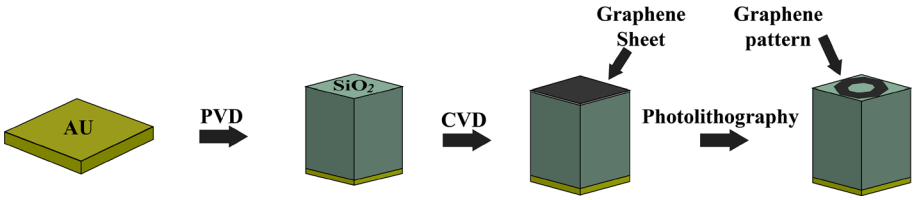

Fig. 13 The fabrication procedure for the proposed sensors

8 Conclusion

In conclusion, this work introduces three graphene-based metamaterial biosensors specifically designed for efficient detection of cancer cells and other biological analytes. The first proposed structure operates as a single-band absorber, while the second and third designs exhibit dual-band absorption characteristics and are polarization-insensitive. Each sensor adopts a straightforward three-layer architecture consisting of a metallic ground plane, a SiO_2 dielectric spacer, and a patterned graphene layer, enabling strong and tunable absorption at terahertz frequencies. Simulation outcomes confirm excellent sensitivity and reliable detection performance across different cancer cell types, emphasizing the role of graphene's tunable chemical potential and optimized geometrical design. The main merits of the proposed biosensors include polarization insensitivity (for the dual-band models), multi-band response, dynamic tunability, and fabrication simplicity. Owing to these advantages, the proposed designs hold significant promise for practical applications in biomedical diagnostics, biosensing, environmental monitoring, and biosecurity systems.

Authors contribution All Author,Saeed Heidary Kamarroodi, Javad Javidan, have equal contribution.

Funding The authors did not receive support from any organization for the submitted work.

Data availability Our submission has no associated data. All data generated or analyzed during this study are included in this published article.

Declarations

Conflict of interest The authors declare no competing interests.

References

Aieta, F., et al.: Aberration-free ultrathin flat lenses and axicons at telecom wavelengths based on plasmonic metasurfaces. Nano Lett. **12**(9), 4932–4936 (2012)

Anwar, S.: Dual-band detection based on metamaterial sensor at terahertz frequency. Opt. Rev. **30**(3), 300–309 (2023)

Baruah, A., et al.: Biomedical applications of graphene-based nanomaterials: recent progress, challenges, and prospects in highly sensitive biosensors. Discover Nano **19**(1), 103 (2024)

Barzegar-Parizi, S., Rejaei, B., Khavasi, A.: Analytical circuit model for periodic arrays of graphene disks. IEEE J. Quantum Electron. **51**(9), 1–7 (2015)

Bi, H., Yang, M., You, R.: Advances in terahertz metasurface graphene for biosensing and application. Discover Nano **18**(1), 63 (2023)

Bose, R., et al., *Applications of graphene and graphene oxide as versatile sensors: a brief review.* Biointerface Res. Appl. Chem., 2023. **13**(457.10): p. 33263.
Cai, W., et al.: Optical cloaking with metamaterials. Nat. Photonics **1**(4), 224–227 (2007)
Cao, T., et al.: Broadband polarization-independent perfect absorber using a phase-change metamaterial at visible frequencies. Sci. Rep. **4**(1), 3955 (2014)
Chalklen, T., Jing, Q., Kar-Narayan, S.: Biosensors based on mechanical and electrical detection techniques. Sensors **20**(19), 5605 (2020)
Chen, P.-Y., Alu, A.: Atomically thin surface cloak using graphene monolayers. ACS Nano **5**(7), 5855–5863 (2011)
Chen, M., et al.: High-efficiency and multi-frequency polarization converters based on graphene metasurface with twisting double L-shaped unit structure array. Opt. Commun. **394**, 50–55 (2017)
Cheng, R., et al.: High-sensitivity biosensor for identification of protein based on terahertz Fano resonance metasurfaces. Opt. Commun. **473**, 125850 (2020)
Fu, M., et al.: Graphene-based tunable dual-frequency terahertz sensor. Nanomaterials **14**(4), 378 (2024)
Gansel, J.K., et al.: Gold helix photonic metamaterial as broadband circular polarizer. Science **325**(5947), 1513–1515 (2009)
Grady, N.K., et al.: Terahertz metamaterials for linear polarization conversion and anomalous refraction. Science **340**(6138), 1304–1307 (2013)
He, L., et al.: A four-narrowband terahertz tunable absorber with perfect absorption and high sensitivity. Mater. Res. Bull. **170**, 112572 (2024)
Huang, C., et al.: Analysis of graphene-based tunable THz four-band absorption sensors. Appl. Opt. **61**(8), 2103–2107 (2022)
Jacob, Z., Alekseyev, L.V., Narimanov, E.: Optical hyperlens: far-field imaging beyond the diffraction limit. Opt. Express **14**(18), 8247–8256 (2006)
Jandas, P., et al.: Highly selective and label-free Love-mode surface acoustic wave biosensor for carcinoembryonic antigen detection using a self-assembled monolayer bioreceptor. Appl. Surf. Sci. **518**, 146061 (2020)
Kafesaki, M., et al.: Left-handed metamaterials: the fishnet structure and its variations. Phys. Rev. B **75**(23), 235114 (2007)
Kawata, S., Ono, A., Verma, P.: Subwavelength colour imaging with a metallic nanolens. Nat. Photonics **2**(7), 438–442 (2008)
Khatami, S.A., et al.: Smith chart analysis for transmission line method validation of a simple graphene-based absorber in sugar molecules detection. Results Phys. (2025a). https://doi.org/10.1016/j.rinp.2025.108464
Khatami, S.A., et al.: Comprehensive sensing framework for sugar molecules based on graphene absorber: coupled mode theory, transmission line analysis, and deep learning integration. Diamond Relat. Mater. (2025b). https://doi.org/10.1016/j.diamond.2025.112934
Khodadadi, B., et al.: Sensitivity increment of metamaterial-based refractive index sensor with silicon layers. SILICON **15**(15), 6745–6759 (2023a)
Khodadadi, B., et al.: Triple-band metamaterial perfect absorber for refractive index sensing in THz frequency. Opt. Quantum Electron. **55**(5), 431 (2023b)
Khodadadi, B., Rezaei, P., Hadipour, S.: Accurate graphene-based absorber for slight leakage detection of Radon and chloroform air-pollution. Results Phys. **71**, 108196 (2025a)
Khodadadi, B., Rezaei, P., Hadipour, S.: Dual-band polarization-independent maze-shaped absorber based on graphene for terahertz biomedical sensing. Opt. Express **33**(3), 3869–3880 (2025b)
Khorasaninejad, M., et al.: Metalenses at visible wavelengths: diffraction-limited focusing and subwavelength resolution imaging. Science **352**(6290), 1190–1194 (2016)
Kumar, N.A., Devi, B.R., Bhimaavarapu, K.: Graphene-infused terahertz metasurfaces for high-sensitivity refractive index sensing with dual-peak absorption. Plasmonics (2025). https://doi.org/10.1007/s11468-025-03035-y
Li, M., Anand, R.K.: Cellular dielectrophoresis coupled with single-cell analysis. Anal. Bioanal. Chem. **410**(10), 2499–2515 (2018)
Linden, S., et al.: Magnetic response of metamaterials at 100 terahertz. Science **306**(5700), 1351–1353 (2004)
Liu, N., et al.: Plasmonic analogue of electromagnetically induced transparency at the Drude damping limit. Nat. Mater. **8**(9), 758–762 (2009)
Liu, X., et al.: Enhanced binding efficiency of microcantilever biosensor for the detection of yersinia. Sensors **19**(15), 3326 (2019)
Liu, T., et al.: Multifunctional terahertz device with active switching between bimodal perfect absorption and plasmon-induced transparency. Mater. Res. Bull. **171**, 112635 (2024)
Lu, X., et al.: Design and analysis of a dual-band THz metamaterial sensor with high refractive index sensitivity. Front. Phys. **10**, 973033 (2022)

Mamoun, H.M., et al.: Design of highly sensitive dual-band THz metamaterial sensor for cancer early detection. Plasmonics (2025). https://doi.org/10.1007/s11468-025-03161-7
Marques, R., et al.: A new 2D isotropic left-handed metamaterial design: theory and experiment. Microw. Opt. Technol. Lett. **35**(5), 405–408 (2002)
Nahid, M.A., et al.: An evaluation of the impact of clinical bacterial isolates on epithelial cell monolayer integrity by the electric Cell-Substrate Impedance Sensing (ECIS) method. J. Microbiol. Methods **169**, 105833 (2020)
Ni, X., Kildishev, A.V., Shalaev, V.M.: Metasurface holograms for visible light. Nat. Commun. **4**(1), 2807 (2013)
Parvin, T., et al.: Differential optical absorption spectroscopy-based refractive index sensor for cancer cell detection. Opt. Rev. **28**(1), 134–143 (2021)
Pilehroudi, A., et al.: Three-band graphene-based fully independent polarization absorber for biosensing applications. Plasmonics **20**(7), 4333–4344 (2025)
Plum, E., et al.: Metamaterials: optical activity without chirality. Phys. Rev. Lett. **102**(11), 113902 (2009)
Poddubny, A., et al.: Hyperbolic metamaterials. Nat. Photonics **7**(12), 948–957 (2013)
Presnova, G., et al.: Biosensor based on a silicon nanowire field-effect transistor functionalized by gold nanoparticles for the highly sensitive determination of prostate specific antigen. Biosens. Bioelectron. **88**, 283–289 (2017)
Rafighirani, Y., Javidan, J.: Revolutionizing early cancer detection: graphene-based terahertz biosensors for precision diagnostics. Plasmonics (2025). https://doi.org/10.1007/s11468-025-03247-2
Rafighirani, Y., Bahador, H., Javidan, J.: Graphene-based LSPR sensors enable polarization-independent detection of CEA antigens. Sci. Rep. **15**(1), 31388 (2025a)
Rafighirani, Y., Javidan, J., Heidarzadeh, H.: Polarization-independent ultra-sensitive graphene sensor for the detection of prostate-specific antigen. Optik **322**, 172196 (2025b)
Razani, A.N., et al.: Absorption-based ultra-sensitive RI sensor based on the flower-shaped graphene resonator for early detection of cancer. Opt. Commun. **524**, 128775 (2022)
Rizzi, F., et al.: Biomimetics of underwater hair cell sensing. Microelectron. Eng. **132**, 90–97 (2015)
Schurig, D., et al.: Metamaterial electromagnetic cloak at microwave frequencies. Science **314**(5801), 977–980 (2006)
Shalaev, V.M.: Optical negative-index metamaterials. Nat. Photonics **1**(1), 41–48 (2007)
Shangguan, Q., et al.: Design of ultra-narrow band graphene refractive index sensor. Sensors **22**(17), 6483 (2022)
Shelby, R.A., Smith, D.R., Schultz, S.: Experimental verification of a negative index of refraction. Science **292**(5514), 77–79 (2001)
Smith, D.R., et al.: Composite medium with simultaneously negative permeability and permittivity. Phys. Rev. Lett. **84**(18), 4184 (2000)
Song, Q., et al.: Water-resonator-based metasurface: an ultrabroadband and near-unity absorption. Adv. Opt. Mater. **5**(8), 1601103 (2017)
Thongrattanasiri, S., Koppens, F.H., de García Abajo, F.J.: Complete optical absorption in periodically patterned graphene. Phys. Rev. Lett. **108**(4), 047401 (2012)
Tian, J., et al.: Tunable quad-band perfect metamaterial absorber on the basis of monolayer graphene pattern and its sensing application. Results Phys. **26**, 104447 (2021)
Valentine, J., et al.: Three-dimensional optical metamaterial with a negative refractive index. Nature **455**(7211), 376–379 (2008)
Valentine, J., et al.: An optical cloak made of dielectrics. Nat. Mater. **8**(7), 568–571 (2009)
Valev, V.K., et al.: Chirality and chiroptical effects in plasmonic nanostructures: fundamentals, recent progress, and outlook. Adv. Mater. **25**(18), 2517–2534 (2013)
Walser, R.M. *Electromagnetic metamaterials*. in *Complex Mediums II: beyond linear isotropic dielectrics*. 2001. SPIE.
Wang, D., et al.: A high Q-factor dual-band terahertz metamaterial absorber and its sensing characteristics. Nanoscale **15**(7), 3398–3407 (2023)
Wekalao, J., et al.: Terahertz optical ultrasensitive glucose detection using graphene and silver surface plasmon resonance metasurfaces for biomedical applications. Plasmonics **20**(1), 373–385 (2025)
Zhang, X., Liu, Z.: Superlenses to overcome the diffraction limit. Nat. Mater. **7**(6), 435–441 (2008)
Zhang, S., et al.: Plasmon-induced transparency in metamaterials. Phys. Rev. Lett. **101**(4), 047401 (2008)
Zhang, W., et al.: A pseudo-planar metasurface for a polarization rotator. Opt. Express **22**(9), 10446–10454 (2014)
Zhang, M., et al.: Tunable polarization conversion and rotation based on a reconfigurable metasurface. Sci. Rep. **7**(1), 12068 (2017)
Zhang, W., et al.: Microfluid-based soft metasurface for tunable optical activity in THz wave. Opt. Express **29**(6), 8786–8795 (2021)

Zhang, W., et al.: An active electromagnetically induced transparency (EIT) metamaterial based on conductive coupling. Materials **15**(20), 7371 (2022a)
Zhang, M., et al.: A reflective metasurface for broadband OAM vortex wave generation. Front. Phys. **10**, 1042024 (2022b)
Zhang, H., et al.: A dual-band terahertz metamaterial sensor with high Q-factor and sensitivity. Opt. Quantum Electron. **55**(13), 1126 (2023)
Zhang, W., et al., *Micromachined switchable metamaterial with dual resonance.* Applied physics letters, 2012. **101**(15).
Zhang, W., et al., *Single mode to dual mode switch through a THz reconfigurable metamaterial.* Applied Physics Letters, 2017. **111**(24).
Zhao, L., et al.: Design of multi-narrowband metamaterial perfect absorbers in near-infrared band based on resonators asymmetric method and modified resonators stacked method. Opt. Commun. **420**, 95–103 (2018)
Zhao, J. and Z. Meng, *High-sensitivity refractive index sensing based on a dual ultra-narrowband terahertz metasurface absorber.* Plasmonics, 2025: p. 1–12.
Zheng, G., et al.: Metasurface holograms reaching 80% efficiency. Nat. Nanotechnol. **10**(4), 308–312 (2015)